Comprehensive Investigation of Thermal and Mechanical Loads on Stator Winding Insulation in Non-salient Synchronous Generator under RISC fault

Kai Sun, *Student Member*, *IEEE,* Yu-Ling He, *Senior Member*, *IEEE*, Hui-Cai Chen, Xue-Wei Wu, Jia-Wen Yang, Guiji Tang, Fengyu Zhang, David Gerada, *Senior Member*, *IEEE*

***Abstract*— Current studies on frequent rotor interturn short circuits (RISC) primarily focus on fault diagnosis. However, the detrimental effect of RISC on the fragile stator winding insulation of synchronous generators is overlooked. Consequently, this article comprehensively investigates thermal and mechanical loads, as well as the structural responses of the stator winding insulation. The impact of RISC fault on the thermal and mechanical degradation distribution patterns of the insulation is explored in detail. Besides, different from the current research on RISC, this study considers a broader range of influencing factors, including the degree, position, contact resistance, and output. In this paper, detailed theoretical models for calculating thermal and mechanical loads are presented. FEA and experiments are conducted on a 5kW synchronous generator to calculate and test thermal and mechanical loads on the insulation. The mechanical, thermal, and coupling structural responses of the insulation are obtained and compared. The results indicate that maximum insulation structural responses caused by mechanical loads, thermal loads, and coupling actions is most pronounced at the nose end and the junction between the straight and involute lines, warranting careful attention. This study offers a unified approach and a practical framework for extended insulation service life.**

***Index Terms*—no-salient synchronous generator, winding insulation, rotor interturn short circuit, thermal and mechanical loads, structural responses**

I. INTRODUCTION

Rotor Inter-turn Short Circuit (RISC) is one of the common electrical faults of synchronous generators. The RISC primarily arises from insulation failure in the field winding due to deficiencies in manufacturing and installation process, aging, thermal and mechanical stress concentration etc. [1-2]. The occurrence of RISC leads to severe consequences, including magnetic field imbalances, abnormal temperature rises [3], and rotor grounding [4-5]. Therefore, studying the RISC in synchronous generators is of great significance.

A review of the existing literature indicates that current methods for detecting RISC fault predominantly rely on changes in parameter characteristics. For example, H. Ehya *et al.* [6] proposed a sparse sensor system that integrates stack classifier with a single air-gap flux sensor for RISC fault detection. Similarly, B. Aubert *et al.* [7] introduced a method employing Kalman filter to identify RISC fault. L. Hao *et al.* [8] developed an online fault monitoring technique based on the effective value of stator branch unbalance current. Concurrently, A. Nysveen *et al.* [9] proposed a detection method utilizing a non-invasive sensor to detect stray magnetic fields. Additionally, M. Cuevas *et al.* [10] conducted a coupling analysis of the stray magnetic field and the external shell vibration. Advanced algorithms, such as digital neural networks [11] and variational pattern decomposition [12] etc., have also been developed for RISC detection. The aforementioned literature emphasizes the RISC fault identification. However, the detrimental effects of RISC on key components of synchronous generators are often overlooked when fault detection is delayed.

Numerous scholars have extensively researched losses in synchronous machine to ensure that temperature rise remains within a reasonable range during operation. For instance, Lian *et al.* [13] examined synchronous motors loss and temperature under various power supply modes. Y. -L. He *et al.* [14] investigated the thermal characteristics of stator winding in the presence of air gap eccentricity. J. Wang *et al.* [15] analyzed the relationship between electromagnetic losses and temperature rise across different motor components. Besides, S. Jia *et al.* [16] studied the loss distribution of synchronous generator under three-phase short-circuit fault. Further, R. Wrobel *et al.* [17] examined the proximity loss in end windings and proposed a correction factor for copper loss. To reduce copper loss, G. Berardi *et al.* [18] introduced a transposition method considering double electric layer. W. Li *et al.* [19-20] analyzed the temperature distribution of sleeves made from various materials, and evaluated fluid flow within the end regio. While the above research provides a solid theoretical foundation and methodological support for calculating generator temperature rise, the impact of RISC on the thermal load of stator winding insulation remains unclear.

In addition, the mechanical properties of synchronous generators, including mechanical force and vibration, also warrant special attention. For instance, the radial vibration force of non-polar synchronous generator is conducted by distributed magnetic circuit method under no-load condition [21]. The stator vibration under different eccentricities in wound-rotor synchronous generators [22] and built-in

This work is supported by National Natural Science Foundation of China (52177042), National Natural Science Foundation of Hebei Province (E2022502003、E2021502038), Chinese Fundamental Research Funds for the Central Universities (2023MS128), High Level Talent Support Program of Hebei Province (B20231006).

Kai Sun (120222102025@ncepu.edu.cn). Yu-Ling He (corresponding author, heyuling1@ncepu.edu.cn). Hui-Cai Chen (220242224073 @ncepu.edu.cn). Xue-Wei Wu (220222224043@ncepu.edu.cn). Jia-Wen Yang (220232224004@ncepu.edu.cn). Guiji Tang (tanggjlk@ncepu.edu.cn) are with Department of Mechanical Engineering, North China Electric Power University, Baoding, 071003, China.

Fengyu Zhang (Fengyu.zhang1@nottingham.ac.uk) and David Gerada (david.gerada@nottingham.ac.uk). are with Department of Electrical and Electronics Engineering, University of Nottingham, Nottingham, NG7 2RD, UK.

permanent magnet synchronous generator [23] are studied in-dept based on air gap permeance method. Meanwhile, comprehensive investigations consider mechanical forces and vibrations of the rotor [24] and the end winding [25], taking into account the stator interturn short-circuit position. In addition, when RISC occurs, the rotor core vibrates at the fundamental frequency, and the vibration amplitude is positively correlated with the RISC degree [26]. In contrast, short-circuit magnetic pull has minimal influence on rotor structural stress [27]. Besides, the occurrence of RISC results in fluctuations in electromagnetic torque [28-30].

However, the aforementioned studies focus on stator/rotor [22-24] cores, stator winding [25] and rotating shaft [28-30]. In contrast, the load assessment and structural response of the fragile insulation in the stator winding have been rarely addressed. As illustrated in Fig. 1, the winding structure is a hollow cylinder whose straight section is securely fixed within the stator core. To facilitate the calculation of load properties, the insulation and the winding are treated as a single entity, respectively. During generator operation, the windings experience electromagnetic forces (EF), which impose mechanical loads on the end insulation. Concurrently, both an internal electrical heat source and an external magnetic heat source elevate the insulation temperature, resulting in a thermal load on the insulation. Besides, traditional research on RISC tends to concentrate on electromagnetic parameters of synchronous generators, including electromagnetic torque [28-29], stator current [8], and stray magnetic fields [9-10], primarily for fault diagnosis. Yet, the impact of RISC on mechanical/thermal loads affecting stator insulation remains unexplored.

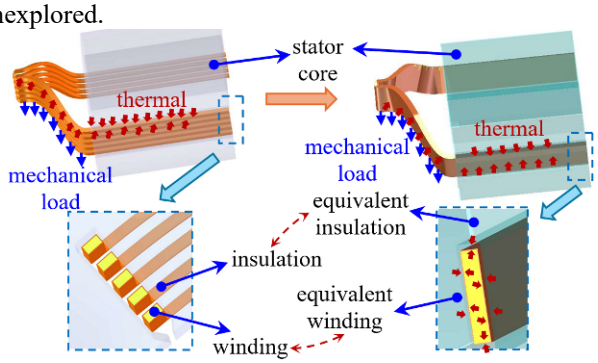

Fig. 1 Equivalent model of generator stator winding and insulation

Motivated by this gap, the paper comprehensively investigates thermal and mechanical loads properties of the stator winding insulation. The influence of RISC on single and coupled insulation structural responses is calculated based on multi-physics coupling. Additionally, prone to deformation and complex stress distributions of stator winding insulation are examined in detail. This study presents three novel contributions:

i) The investigation of thermal and mechanical loads on insulation under RISC cases introduces innovative analysis. The thermal load considers not only the non-equilibrium electrical heat source within the insulation but also the non-uniform magnetic heat source external to it.

ii) The structural responses of the insulation, both single and coupled, are ingeniously derived under the influence of thermal and mechanical loads. The patterns of thermal/mechanical degradation, along with important locations influenced by RISC, are identified, providing common idea and viable strategies for preventing possible insulation failures.

iii) Different from current research on RISC, which typically considers two influencing factors (RISC degree [6-9], [26-27] and position [28-29], [31]), this paper analyzes the effects of four influencing factors on RISC.

This article is organized as follows. Section II presents theoretical calculation models of thermal and mechanical loads in detail. Section III describes the finite element analysis (FEA) and experiments conducted on a 5kW synchronous generator to calculate and test the thermal and mechanical loads on the insulation. The mechanical, thermal, and coupled structural responses of the insulation are obtained. Section IV finally concludes this work.

II. Theorical Model for Thermal and Mechanical Load Analysis

A. MFD calculation under RISC cases

Magnetic flux density (MFD) is a fundamental parameter closely associated with thermal and mechanical loads experienced key components of synchronous generator. Generally, the air gap MFD is obtained by the magnetomotive force (MMF) and the permeance per unit area. The MFD can be expressed as (1).

$$B(\alpha_m,t)=f(\alpha_m,t)\Lambda_0 \tag{1}$$

where α_m is the mechanical circumferential angle that characterizes the air-gap position, t denotes time. B, f and Λ_0 denote MFD, MMF and permeance per unit area.

In the RISC case, the field winding in the short circuit slot is divided into two parts: the normal part and the short circuit part, as depicted in Fig. 2(a). The corresponding equivalent circuit of the field winding under the RISC case is shown in Fig. 2(b). Here, α_r indicates the RISC position. R_s, R_n and R_f represent the resistance of the short circuit part, the normal part and the contact resistance, respectively. The current in short circuit winding, normal winding, and R_f are denoted as I_{sh}, I_n and I_f, respectively. It can be seen that excited current under the RISC case flows through R_f. Thus, the RISC case can be viewed as the normal case with a superimposed reverse DC I_f in the short circuit. Ignoring the inductance in the rotor DC circuit, I_f is expressed by (2).

$$I_f=\frac{R_sI_n}{R_f+R_s} \tag{2}$$

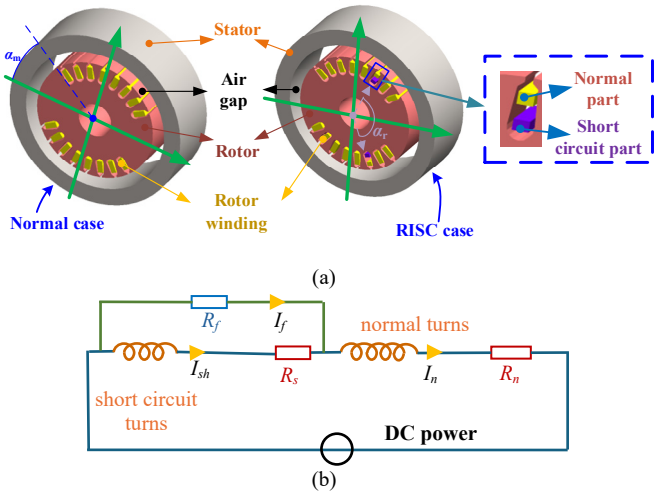

Fig. 2 Synchronous generator under RISC case: (a) physical model, (b) equivalent circuit of field winding under RISC case

Further, the MMF of the rotor winding under the normal case can be expressed as odd harmonics with amplitude a, as shown in Fig. 3. In the RISC case, a portion of the rotor

winding current flows through the resistance R_f. Based on the current distribution, the MMF under the RISC case can be equivalent to the MMF under the normal superimposed with a reverse MMF, which is generated by the current I_f [28-29], [32]. According to the Gauss flux theorem, the positive MMF must cover the same area as the negative MMF. As a result, the MMF under the RISC will be compressed, with the peak and the valley values reduced by δ_1 and δ_2, respectively. Specially, the Reverse MMF $f_d(\alpha_m, t)$ can be expressed by (3).

$$\begin{cases} f_d(\alpha_m, t) = \sum_n F_{dn} \cos(np\omega t - np\alpha_m - \varphi_n) \\ F_{dn} = \dfrac{2I_f n_m}{n\pi} \sin\dfrac{n\alpha_r}{2} \end{cases} \tag{3}$$

where n_m is the number of short circuit turns, characterizing the RISC degree. n is positive integer. p is poles number of synchronous generators. ω is the mechanical angular velocity. F_{dn} and φ_n is amplitude and phase angle of n^{th} harmonic MMF.

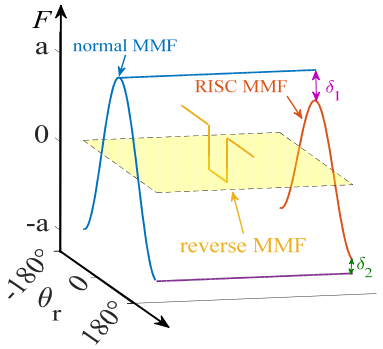

Fig. 3 Rotor winding MMF diagram under different cases

Air gap MMF is the vector sum of the rotor MMF and the stator MMF. For clarity, Fig. 4(a) shows the spatiotemporal relationship of MMF harmonics. Air gap MMF expression under the normal and RISC case is obtained by [8], [28] as (4).

$$f(\alpha_m, t) = \begin{cases} \sum_\gamma F_{s\gamma} \cos(\gamma p\omega t - \gamma p\alpha_m - \psi - \dfrac{\pi}{2}) + \sum_\gamma F_{r\gamma} \cos(\gamma p\omega t - \gamma p\alpha_m) \\ \quad = \sum_\gamma F_{c\gamma} \cos(\gamma p\omega t - \gamma p\alpha_m - \beta_\gamma) \cdots\cdots \text{normal} \\ \sum_\gamma F_{s\gamma 1} \cos(\gamma p\omega t - \gamma p\alpha_m - \psi - \dfrac{\pi}{2}) + \sum_\gamma F_{r\gamma} \cos(\gamma p\omega t - \gamma p\alpha_m) \\ -\sum_n F_{dn} \cos(np\omega t - np\alpha_m - \varphi_n) \\ \quad = \sum_\gamma F_{c\gamma 1} \cos(\gamma p\omega t - \gamma p\alpha_m - \beta_{\gamma 1}) - \sum_k F_{dk} \cos(kp\omega t - kp\alpha_m - \varphi_k) \\ \quad \cdots\cdots \text{RISC} \end{cases} \tag{4}$$

where γ and k are odd and even integers, indicating the MMF harmonic order. $F_{s\gamma}$, $F_{r\gamma}$ and $F_{c\gamma}$ are γth-harmonic amplitude of stator MMF, rotor MMF and composite MMF under normal case, respectively. $F_{s\gamma 1}$ and $F_{c\gamma 1}$ are γth-harmonic amplitude of stator MMF and composite MMF under RISC case. β_γ and $\beta_{\gamma 1}$ are the phase angle of composite MMF γth-harmonic under normal and RISC case, respectively.

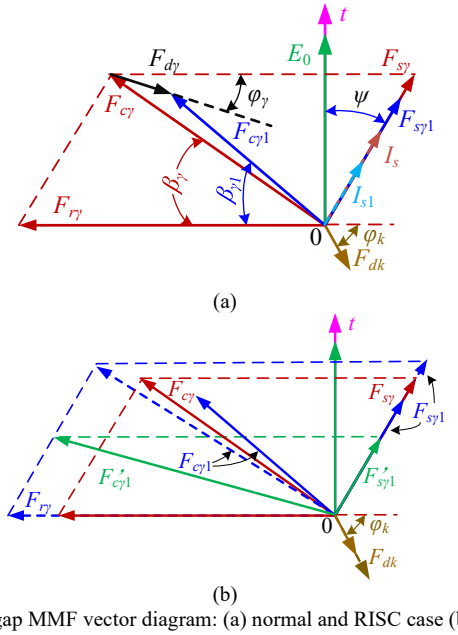

Fig. 4 Air gap MMF vector diagram: (a) normal and RISC case (b) RISC considering forced excitation

For non-salient synchronous generator, the air gap is uniformly distributed, so the permeance per unit area Λ_0 remains constant. According to (1), both the MFD and the MMF exhibit similar properties. Furthermore, based on (4), the MFD is predominantly influenced by odd harmonics under the normal case. When the RISC occurs, the even harmonics appear in the MFD spectrum, while the amplitudes of odd harmonics decrease ($F_{c\gamma 1} < F_{c\gamma}$). Generally, the RISC weakens the air gap MMF, resulting in a reduction in the output voltage of the synchronous generator. To compensate for this, the excitation current must be increased to maintain energy conservation and constant terminal voltage. In essence, the synchronous generator initiates forced excitation [33]. The greater the weakening of the magnetic field, the higher the required excitation current. Under forced excitation condition, the MMF increases, as indicated by the dotted arrow in Fig. 4(b), $F_{c\gamma 1} > F_{c\gamma}$. Additionally, the output also affects the air gap MMF amplitude, as the stator MMF amplitude is obviously correlated with phase current, according to per Ampère's circuital law. In Fig. 4(b), $F'_{s\gamma 1}$ and $F'_{c\gamma 1}$ are γth-harmonic amplitude of stator MMF and composite MMF under the RISC with half output case. $F_{r\gamma}$ denotes the air gap MMF under no output case. $F_{c\gamma 1} < F'_{c\gamma 1} < F_{r\gamma}$. As the output decreases, the odd harmonics amplitudes of air gap MMF increases.

Based on the aforementioned analysis, it is evident that the air gap MMF/MFD under the RISC cases is influenced by four factors: the RISC degree (n_m), the RISC position (α_r), the output (F_s) and the contact resistance (R_f). Considering forced excitation, the findings are as follows: 1) As n_r increase, all harmonics amplitudes increase. 2) An increase in R_f reduces reversed current amplitude, consequently increasing air gap MMF amplitude as R_f decreases. 3) Increasing α_r leads to an increase in each harmonic amplitude. 4) A reduction in output increases odd harmonics amplitudes and has minimal effect on even harmonics.

B. Impact of RISC on insulation thermal load

During the operation of synchronous generators, the windings within the insulation and the stator core external

to the insulation contribute to the copper loss and the core loss, respectively. The combined effects of the heat produced by external the core loss and internal the copper loss lead to an uneven temperature distribution within the insulation. Consequently, the insulation experiences unbalanced and undesirable thermal loads.

Currently, the core loss is calculated using Bertotti's iron-loss model, where the core loss P_{Fe} is divided into the hysteresis loss P_H, the eddy current loss P_C and the excess loss P_E. The P_{Fe} expression can be written as (5).

$$P_{Fe} = P_H + P_C + P_E = k_h f_1 B^{\alpha} + k_e f_1^{\,2} B^2 + k_a f_1^{\,1.5} B^{1.5}$$
$$= \begin{cases} 0.159\omega k_h \Lambda_0^2 \sum\limits_{\gamma} \gamma F_{c\gamma}^2 + 0.025\omega^2 k_e \Lambda_0^2 \sum\limits_{\gamma} \gamma^2 F_{c\gamma}^2 \\ +0.063\omega^{1.5} k_a \Lambda_0^{1.5} \sum\limits_{\gamma} \gamma^{1.5} F_{c\gamma}^{1.5} \\ \cdots\cdots\cdots\cdots\cdots\cdots\cdots\cdots\cdots\cdots \text{normal} \\ 0.159\omega k_h \Lambda_0^2 (\sum\limits_{\gamma} \gamma F_{c\gamma 1}^2 + \sum\limits_{k} k F_{dk}^2) + 0.025\omega^2 k_e \Lambda_0^2 (\sum\limits_{\gamma} \gamma^2 F_{c\gamma 1}^2 + \sum\limits_{k} k^2 F_{dk}^2) \\ +0.063\omega^{1.5} k_a \Lambda_0^{1.5} (\sum\limits_{\gamma} \gamma^{1.5} F_{c\gamma 1}^{1.5} + \sum\limits_{k} k^{1.5} F_{dk}^{1.5}) \\ \cdots\cdots\cdots\cdots\cdots\cdots\cdots\cdots\cdots\cdots \text{RISC} \end{cases} \tag{5}$$

where k_h, k_e and k_a are the coefficients of hysteresis loss, eddy current loss and excess loss. f_1 is the magnetic field frequency, B is the air gap MFD amplitude. α is the Steinmetz coefficient, typically set to 2.

Besides, the copper loss, resulting from the thermal effect of the current, also significantly affects the thermal load on the insulation. Given that the skin effect relies on the high frequency currents while higher-order harmonic amplitudes are comparatively smaller, this paper neglects the skin effect. The copper loss P_{Cu} can be expressed as (6).

$$P_{Cu} = 3\sum_{\gamma} I_{s\gamma}^2 R \tag{6}$$

where R denotes the phase winding resistance, $I_{s\gamma}$ is the current RMS of γ-th harmonic. According to the electromagnetic induction law, the instantaneous phase current $i(\alpha_m, t)$ can be written as (7).

$$i(\alpha_m, t) = q w_c k_w B(\alpha_m, t) L v / Z =$$
$$\begin{cases} \dfrac{q w_c \Lambda_0 L \tau \omega}{\pi Z} \sum\limits_{\gamma} k_{w\gamma} F_{c\gamma} \cos(\gamma p \omega t - \gamma p \alpha_m - \beta_{\gamma}) \cdots\cdots\cdots \text{normal} \\ \dfrac{q w_c \Lambda_0 L \tau \omega}{\pi Z} (\sum\limits_{\gamma} k_{w\gamma} F_{c\gamma 1} \cos(\gamma p \omega t - \gamma p \alpha_m - \beta_{\gamma 1}) \\ -\sum\limits_{k} k_{wk} F_{dk} \cos(k p \omega t - k p \alpha_m - \varphi_k)) \cdots\cdots\cdots \text{RISC} \\ k_{w\gamma} = k_{yy} \times k_{q\eta} = \sin\gamma\left(90^{\circ} \times y / \tau\right) \times \sin\left(q\gamma\alpha_1 / 2\right) / \left(q \sin\left(\gamma\alpha_1 / 2\right)\right) \end{cases} \tag{7}$$

where L is the effective length of the stator winding, q is the slot number of each pole in each phase, w_c is the turn number of each winding, $k_{\omega\gamma}$ is the γ-th harmonic winding factor, k_{yy} is the γ-th harmonic pitch factor, $k_{q\eta}$ is the γ-th harmonic distribution factor, α_1 is the angle between two slots, and Z is the external electrical load impedance, which measures the output of the synchronous generator.

When the RISC occurs, new harmonics emerge in the magnetic field of the synchronous generator, and the amplitude of these harmonics increases considering the forced excitation condition. Therefore, based on (5)-(7), both the core loss and the copper loss under the RISC cases exceed those under the normal case. Consequently, insulation temperature rise under the RISC case will be higher than that under the normal, assuming equivalent heat dissipation condition. Moreover, the variation in losses due to the RISC occurrence is consistent with the trends of air gap MFD considering varying RISC degree, position, and contact resistance. Specifically, the copper loss is primarily influenced by the phase current, which correlates with the output. A reduction in output leads to a sharp decrease in the copper loss, while the core loss may increase slightly.

To more accurately calculate the temperature rise of the insulation, this paper analyzes the entire core - insulation - winding system. The strand winding model is simplified, as shown in Fig. 1. The heat conductivity coefficient of this equivalent insulation is given by (8).

$$\lambda_{eq} = \sum_{i=1}^{n} d_i \Big/ \left(\sum_{i=1}^{n} \frac{d_i}{\lambda_i} \right) \tag{8}$$

where λ_{eq} is the heat conductivity coefficient of the equivalent insulation, d_i is the insulation thickness, and λ_i is the heat conductivity coefficient of the each wire insulation.

The core loss and the copper loss serve as internal heat sources affecting the temperature distribution. The paper employs the three-dimensional temperature field analysis method of internal heat source. In the three-dimensional Cartesian coordinate system, the heat energy transfer can be written as (9) [14], [20].

$$\begin{cases} \dfrac{\partial}{\partial x}(\lambda_x \dfrac{\partial T}{\partial x}) + \dfrac{\partial}{\partial y}(\lambda_y \dfrac{\partial T}{\partial y}) + \dfrac{\partial}{\partial z}(\lambda_z \dfrac{\partial T}{\partial z}) + q_v = \rho c \dfrac{\partial T}{\partial t} \\ -\lambda_n \dfrac{\partial T}{\partial x} = \alpha_2 (T - T_f) \end{cases} \tag{9}$$

where λ_x, λ_y, λ_z and λ_n are the thermal conductivity along x-, y-, z- and n-direction, respectively. ρ is the material density, α_2 is the heat dissipation coefficient, c is the specific heat capacity, q_v is the heat density of internal heat source, T and T_f are the temperature of body and surrounding medium.

To facilitate the temperature model solution of the stator system, several assumptions are made:

(1) Influence of heat transfer between stator and rotor is negligible due to high thermal resistance of air gap.

(2) Each conductive medium is considered isotropic.

(3) Magnetic properties of core material remain constant.

Additionally, careful consideration must be given to the boundary conditions of the temperature field. Based on the system's physical structure, the heat exchange modes between winding, insulation, and core involve heat transfer, while the surfaces of insulation and core engage in heat convection. The heat dissipation coefficients for each boundary must be determined for surfaces where convective heat transfer occurs, including the outer surface, end surface, inner surface of the core, and insulation end surface. The corresponding convective heat transfer coefficients are denoted as C_1, C_2, C_3 and C_4, respectively, as shown in Fig. 5. The coefficients can be expressed using empirical formulas as (10) [14], [34].

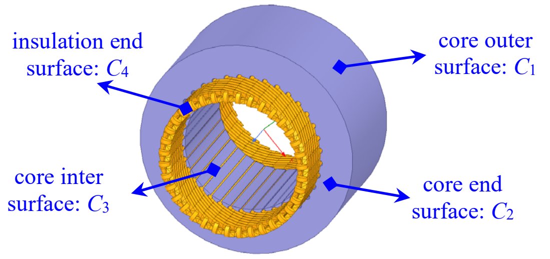

Fig. 5 Convective heat transfer on system surface

$$\begin{cases} C_1 = 9.73 + 14 v_1^{0.62} \\ C_2 = 15 + 6.5 v_2^{0.7} \\ C_3 = 25 + 12.5 v_2^{0.7} \\ C_4 = \dfrac{0.456 \lambda_a Re_t^{0.6}}{d_{et}} \\ Re_t = \dfrac{\pi^2 (D_1 + D_{i1}) d_{et}}{60 \omega \xi} \end{cases} \tag{10}$$

where v_1 is the wind speed on the stator core outer surface, v_2 is the linear speed on the rotor surface. d_{et} is the equivalent diameter of the stator winding end, Re_t is the airflow Reynolds number at the end of winding, λ_a is thermal conductivity of air, D_1 and D_{i1} are the outer diameters and the inner diameter of the stator core, ξ is the viscosity coefficient of air motion.

The system temperature rise induces thermal responses in the insulation, including thermal deformation and thermal stress. Excessive thermal responses may lead to insulation rupture and material carbonization. The thermal deformation of winding insulation can be derived by solving force balance based on the system temperature field distribution. The specific expression is given by (11) [35].

$$\begin{cases} (\sum_1^n \int_V S^T D_s B dv) \bullet U = \sum_1^n \int_V S^T D_s \varepsilon_0 dv \\ \varepsilon_0 = \Delta T \left[\alpha_x, \alpha_y, \alpha_z, 0, 0, 0 \right]^T \\ \sigma = D_s \bullet (\varepsilon - \varepsilon_0) \\ \varepsilon = S \bullet U \end{cases} \tag{11}$$

where S is the element stress matrix, D_s is the elastic stiffness matrix, U is the node displacement vector matrix, ε_0 is the unit thermal strain matrix, ΔT is the temperature rise, α_x, α_y, α_z are the thermal expansion coefficients of each material in x, y, z directions respectively, ε is the total strain matrix, σ is the stress vector.

C. *Impact of RISC on mechanical load*

According to Ampere's force law, the stator winding experiences alternating radial EF. Consequently, the insulation surrounding the winding is subjected to mechanical loads, as depicted in Fig. 6. In response, the insulation undergoes mechanical deformation and stress. On the macro level, the periodic mechanical deformation of the insulation is characterized by the periodic displacement, that is, the vibration. The EF $F_e(\alpha_m, t)$ can be written as (12).

$$\begin{aligned} F_e(\alpha_m, t) &= \int_0^l B_l(\alpha_m, t) i(\alpha_m, t) \cos(\alpha_l) \sin(\beta_l) dl \\ &= \int_0^l \eta B(\alpha_m, t) i(\alpha_m, t) \cos(\alpha_l) \sin(\beta_l) dl \\ &= \eta B(\alpha_m, t) i(\alpha_m, t) l \end{aligned} \tag{12}$$

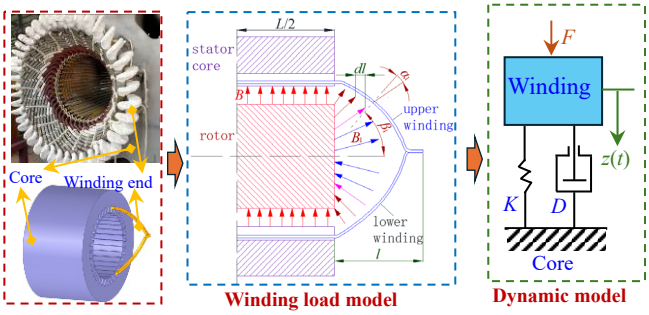

Fig. 6 End winding structure, load and dynamic model

where l is axial length of the winding end part, $B_l(\alpha_m, t)$ is the air gap MFD in the end region. α_l is the angle between the normal line of the calculated end part point and the rotor axis. Substituting (1), (7) to (12), the EF under the normal case and the RISC case can be represented as (13).

$$F_e(\alpha_m, t) = \begin{cases} 0.5A \sum_\gamma k_{w\gamma} F_{c\gamma}^2 + 0.5A \sum_\gamma k_{w\gamma} F_{c\gamma}^2 \cos(2\gamma p\omega t - 2\gamma p\alpha_m - 2\beta_\gamma) \\ \cdots\cdots\cdots\cdots\cdots\cdots\cdots\cdots\cdots\cdots\cdots\cdots\cdots\cdots\cdots\cdots \text{normal} \\ 0.5A \sum_\gamma k_{w\gamma} F_{c\gamma 1}^2 + 0.5A \sum_k k_{wk} F_{dk}^2 \\ +0.5A \sum_\gamma k_{w\gamma} F_{c\gamma 1}^2 \cos(2\gamma p\omega t - 2\gamma p\alpha_m - 2\beta_{\gamma 1}) \\ +0.5A \sum_k k_{wk} F_{dk}^2 + 0.5A \sum_k k_{wk} F_{dk}^2 \cos(2kp\omega t - 2kp\alpha_m - 2\varphi_k) \\ -0.5A \sum_\gamma \sum_k (k_{w\gamma} + k_{wk}) F_{c\gamma 1} F_{dk} \cos((\gamma + k) p\omega t - (\gamma + k) p\alpha_m - \beta_{\gamma 1} - \varphi_k) \\ -0.5A \sum_\gamma \sum_k (k_{w\gamma} + k_{wk}) F_{c\gamma 1} F_{dk} \cos((\gamma - k) p\omega t - (\gamma - k) p\alpha_m - \beta_{\gamma 1} + \varphi_k) \\ \cdots\cdots\cdots\cdots\cdots\cdots\cdots\cdots\cdots\cdots\cdots\cdots\cdots\cdots\cdots\cdots RISC \\ A = \dfrac{q w_c \Lambda_0^2 L \tau \omega \eta l}{\pi Z} \end{cases} \tag{13}$$

As indicated in (13), the EF acting on the winding primarily comprises DC and even harmonic components (2γ) under the normal case. However, additional odd harmonics (γ+k, γ-k) emerge following the occurrence of the RISC. Furthermore, the EF amplitude of each harmonic is predominantly influenced by the air gap MMF amplitude and the output. For constant output, an increase in n_m and α_r, or a decrease in R_f, will enhance the EF. This leads to an increased mechanical load on the insulation. Conversely, as the output rises (Z decreases), the EF also increases significantly.

Additionally, the EF can induce periodic motion in the end winding, resulting in radial vibrations in the end insulation, as shown in Fig. 6. The insulated end can be modeled as a cantilever beam structure, described by the kinetics equation expressed in (14).

$$\begin{cases} \{F_e(t)\} = [M]\{a\} \\ \{F_e(t)\} = \{F_e(t)\} - \{F_D(t)\} - \{F_K(t)\} \\ a = \ddot{x}(t) \\ \{F_D(t)\} = [D]\left\{\dot{x}(t)\right\} \\ \{F_K(t)\} = [K]\{x(t)\} \end{cases} \tag{14}$$

where M is the mass matrix of the end winding, D is the damping matrix provided by the tie lines, K is the stiffness matrix, F_D(t) and $F_K(t)$ are the resistance force matrixes from damping and elastic spring, respectively, and $x(t)$ is the displacement matrix.

According to the mechanical dynamic model, both the input and the output of a mechanical system are co-frequency and positive. In this study, the FE is the input and the resulting vibration is the output. Theoretically, the frequency of the insulation vibration corresponds to the time-varying mechanical loads, including 1st, 2nd, 3rd and 4th harmonics under the RISC cases. Moreover, the greater the FE acting on the insulation, the more intense the insulation vibration.

Besides, as shown in Fig. 7, the mechanical stress is generated in the end insulation under the action of the EF. The mechanical stress in end insulation can be computed through the EF density in (15).

$$\sigma_m = M_1 y / I_z = y \int_0^s F_j ds / I_z = y \int_0^s \int_0^s F_e ds ds / I_z \tag{15}$$

where s is the distance from winding nose end to analyzed cross-section, M_1 is the bending moment at the section, y is

the distance from a point in the cross-section to the neutral axis, I_z is the moment of inertia, F_j is section shear.

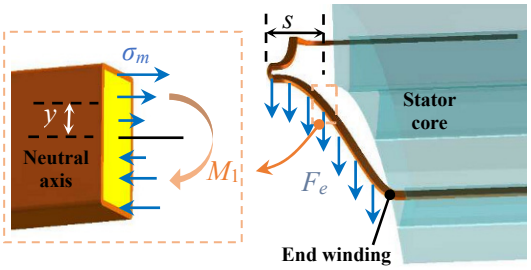

Fig. 7 Schematic diagram of mechanical stress distribution in end winding

The EF in the end winding is unevenly distributed. The farther from the nose, the greater the accumulated bending moment and cross-section stress. Consequently, the stress at the root of the end winding increases, leading to significant changes in the geometry of the winding nose and the onset of stress concentration. The maximum displacement and deformation occur at the insulation nose, as this location is farthest from the fixed support. This results in stress and deformation levels exceeding those in other regions during generator operation. Meanwhile, as shown in Fig. 7, increasing the mechanical load on the end insulation leads to higher maximum stress value.

In summary, since the insulation fully and cohesively contacts the winding, the EF of the winding can be considered as the mechanical load borne by the insulation. Both the vibration and the mechanical stress are characterized by the mechanical response of the insulation to this load. The vibration represents the external expression of the insulation's response, as calculated using (14), while the stress is the result of the internal force in the insulation under the mechanical load, as described by (15). Consequently, the three variables in the studied system can be reliably transformed between them. Specially, the mechanical load, the vibration and the stress exhibit a positive correlation: as the mechanical load increases, both the vibration and the mechanical stress also increase.

III. FEA Calculation and Experimental Validation

A. FEA and experiment setup

To validate the theoretical analysis, a non-salient synchronous generator is subjected to FEA calculations and experiment. This generator, designed and manufactured by the authors to simulate various RISC cases, has its primary parameters outlined in Table I.

TABLE I
Electro-mechanical Parameters of Studied Generator

Parameters	Values	Parameters	Values
rated power	5kVA	stator core length	130mm
power factor(cosφ)	0.8	rated excited current	7.9A
radial air-gap length	1.2mm	rotor slots	16
stator slots	36	rotor core outer diameter	142.6mm
stator outer diameter	250.5mm	rotor core inner diameter	40mm
stator inner diameter	145mm	rotor coil turns per slot	60

The simulation calculations are conducted using Ansys Workbench. As illustrated in Fig. 8(a), a high-fidelity FEA model is established. On the physical model, the rotor winding is divided into normal part and short circuit part. The corresponding external coupled circuit is depicted on the right side of Fig. 8(a). Different degrees and positions of RISC are realized by adjusting short-circuit turns and slots. Output variations are achieved by modifying the electrical load in the external circuit. Additionally, several cases involving contact resistance are considered. Fig. 8(b) presents the coupling paths and calculated parameters for the electromagnetic, thermal, and structural fields. Path 1 pertains to thermal load characteristics, where loss data is input into the temperature field, subsequently informing the structural field to derive thermal responses. In contrast, Path 2 directly represents mechanical load, where mechanical responses are derived based on the EF. The coupling response results from the superposition of these two loads. Furthermore, the material parameters of the synchronous generator key components are illustrated in Table II.

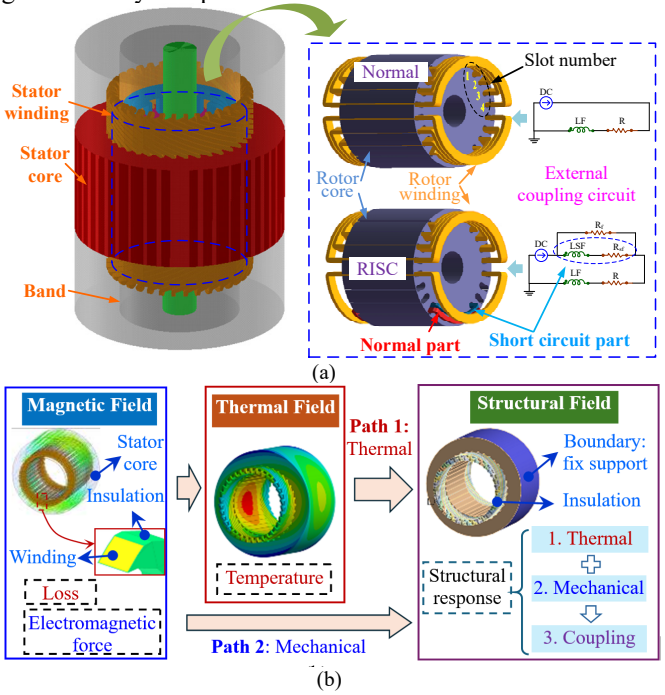

Fig. 8 FEA settings: (a) FEA model, (b) magnetic-thermal-structural field coupling

TABLE II
Material Parameters of Studied Generator

Component	Material name	Young modulus (GPa)	Thermal conductivity W/(m·K)	Thermal expansion (1/K)	Poisson ratio
Stator core	silicon steel	200 (in *radial*) 80 (in *axial*)	60.5	$1.20*10^{-5}$	0.30
Winding	copper	110	396.7	$1.67*10^{-5}$	0.34
Insulation	mica	56	0.34	$8.25*10^{-6}$	0.25

Experimental validation is conducted on a non-salient prototype generator, consistent with the FEA setup, as shown in Fig. 9(a). Specific RISC positions are connected to terminals on the short-circuit tap panel. The temperature rises in the stator core and the insulation are measured using a temperature monitor with K-type thermocouples. Temperature measurement points are located at the end (points 5, 7, 9 and 11), the straight section (points 6, 8, 10 and 12) of the insulation, and the end face (points 1-4) of the stator core, as indicated in Fig. 9(b). The temperature data by monitor device is recorded at a frequency of 0.1Hz.

Ideally, the mechanical load on the end insulation should be directly tested in the experiment. However, given the challenges in directly testing the EF in the winding, the vibration is commonly examined as a proxy for EF measurement. In practice, the acceleration sensors are frequently employed to monitor vibrations due to their small size and ease of installation. The radial vibration of the stator winding is captured using piezoelectricity acceleration sensors (Sensitivity: 10 mV/(m·s^{-2})), which are affixed to the end winding with specialized adhesive and output the voltage signal. The vibration signal by the data

collector is set to a sampling frequency of 10 kHz.

In this study, four groups of RISC cases are analyzed in addition to the normal case. Specially, the RISC case with 5% degree, position in slot 2 and 0.0001 Ω R_f, accompanied by the full output is set to a comparison case. In all the tables of the paper, the 5% degree, the slot 2, the 0.0001 Ω, and the full output is same case, which refers to the comparison case. Compared with comparison case, only the parameter value of single influencing factor is changed in the other RISC cases, which are as follows: 1) varying short-circuit degree (5% (L1-L2), 10% (L1-L3), and 15% (L1-L4)), 2) varying short-circuit positions (slot 2, slot 3, and slot 4), 3) varying output (no, half, and full output), and 4) varying contact resistances (0.0001 Ω, 0.5 Ω, and 1 Ω). Besides, the excitation current under different RISC cases is shown in Table III.

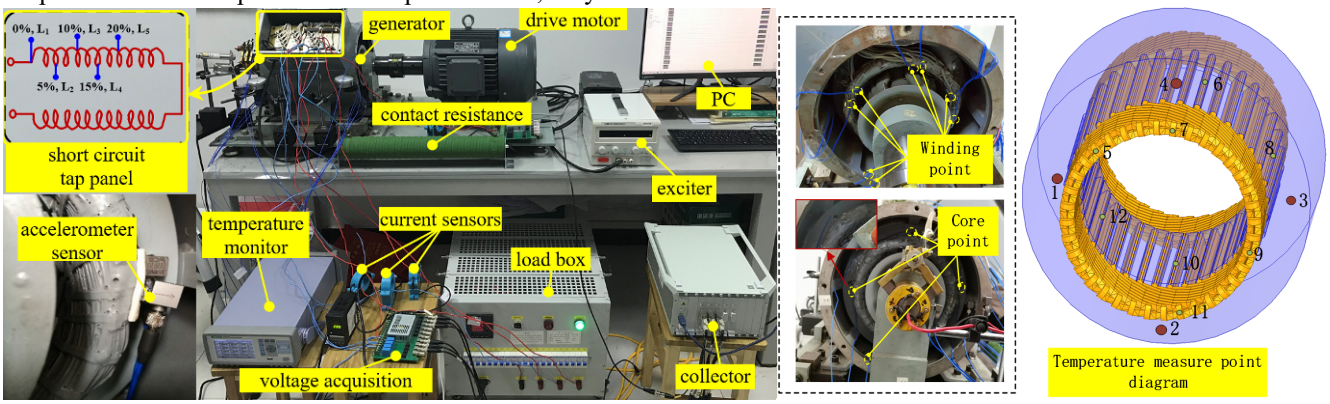

(a) (b)

Fig. 9 RISC fault experiment: (a) experiment platform (b) temperature measure points

TABLE III
Excitation Current under Different RISC Cases

Case	0	5%	10%	15%	Slot2	Slot3	Slot4	Full	Half	No	0.0001Ω	0.5Ω	1Ω
Excited current (A)	7.9	8.92	9.58	10.23	8.92	9.15	9.31	8.92	8.92	8.92	8.92	8.73	8.58

B. *MFD results*

Fig. 10 displays the air gap MFD time curves and spectra obtained from FEA calculations under different RISC cases. The results indicate that the RISC introduces new even harmonics in the air gap MFD compared to normal. Fig. 9(a) clearly illustrates the rapid increase in MFD amplitude with increasing RISC degrees. Similarly, the farther the short-circuit position is from the large tooth (from slot 2 to slot 4), the greater the MFD amplitude, as depicted in Fig. 10(b). Correspondingly, the amplitudes of the contained harmonics, including 1st, 2nd, 3rd and 4th harmonics, follow the same variation trend. Additionally, observing the curves in Fig. 10(c), The values of the air gap MFD under three output cases exhibit a dynamic relationship that varies with the passage of time. For instance, during the time interval from 0.01s to 0.02s, the no-output curve attains the highest magnitude initially. Subsequently, the half-output curve follows, and ultimately, the full-output curve demonstrates the largest amplitude. This phenomenon can be attributed to the fact that as the output/stator current increases, the stator MMF will be increased as well. Concomitantly, the air gap MMF experiences a phase lag along the time (see Fig. 4, $\beta_{\gamma 1}$ increases as the output increases). Notably, the spectrum under varying output cases shows that output variations significantly affect odd harmonics but have minimal impact on even harmonics. The reasons for this phenomenon are explained as follows. The normal stator current has only odd harmonics and does not include even harmonics due to the DC excitation (the step wave of the rotor MMF can be only decomposed to odd harmonics by Fourier Series). Hence, the stator MMF contains the same odd harmonics components. When the output increases, the odd harmonic amplitudes of the phase current and the stator MMF will be also increased. However, the rotor MMF in the RISC cases includes both odd and even harmonics (the extra even harmonics are produced by RISC) [28]. Since the armature reaction will decrease the composite air gap MMF $F_{c\gamma}$ due to the obtuse angle between $F_{r\gamma}$ and $F_{s\gamma}$ (see Fig.4), the increment of the output will enlarge $F_{s\gamma}$ but decrease $F_{c\gamma}$. Consequently, the odd harmonics of MFD will be decreased. On the contrary, the even harmonics only depend on the RISC and the exciting current. They will generally keep the same since neither the RISC effect nor the exciting current is increased. Besides, Fig. 10(d) demonstrate that an increase in contact resistance results in a reduction of MFD. in summary, the observed variation trend of MFD aligns with the theoretical analysis.

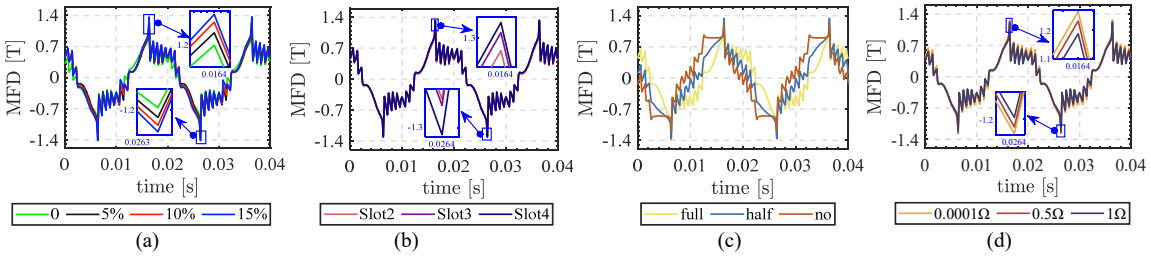

(a) (b) (c) (d)

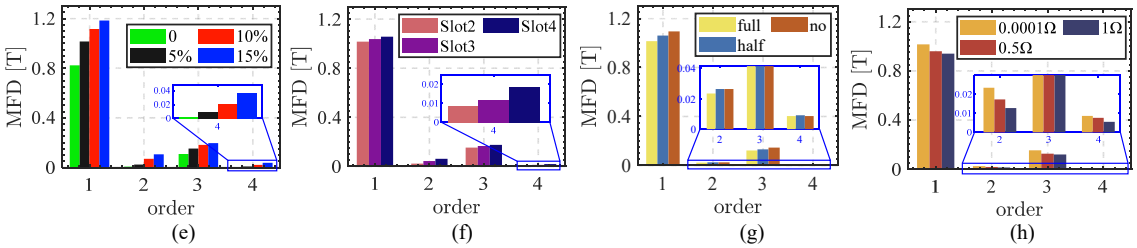

Fig. 10 air gap MFD by FEA: (a) to (d) curves and (e) to (h) spectrum under varied short circuit degrees, varied positions, varied output, varied contact resistance

C. Thermal load results

Fig. 11 shows the core loss and the copper loss calculated through theoretical model and FEA under various RISC cases. The core loss encompasses hysteresis loss and eddy current loss, while excess loss is neglected. The results indicate that hysteresis loss is considerably larger than eddy current loss in the stator core. Additionally, core loss is slightly lower than copper loss in the winding. When comparing losses across different RISC cases, an increase in short-circuit degree, a greater distance of the RISC position from rotor large tooth, or a reduction in R_f leads to an increase in all losses. For example, the core loss under RISC 15% case is 66.4 W (as per FEA) and 89.6 W (according to the theoretical model), which is higher than that under normal case. Meanwhile, reducing the output results in a significant decrease in copper loss due to a sharp reduction in phase current. Overall, the results from the theoretical model correlate well with the simulation results.

Furthermore, the temperature rise of the stator core, the winding and the insulation is calculated by the FEA to assess the thermal load on the insulation. Firstly, the copper loss and the core loss are integrated into the temperature field as internal and external heat sources for the insulation, respectively. Then, the boundary conditions of the temperature field are set according to Fig. 5. Besides, the initial temperature set at 18°C based on actual conditions. The system reaches a steady state within 20 minutes.

Fig. 12 illustrates the simulation results showing the temperature distribution across the core-winding and the insulation thermal load under partial RISC cases. Fig. 13(a) and (b) display the experimental temperature measurements at point 10, recorded by a thermocouple. Fig. 13(c) and (d) illustrate the maximum temperature variations at three key locations: the insulation middle, the insulation end, and the core end face, under varying RISC degrees and contact resistance. These locations are designated as Position 1, 2, and 3, respectively. The temperature at Position 1 is the average of measurements taken at points 6, 8, 10, and 12, while Position 2 averages the measurements at points 5, 7, 9, and 11. Position 3 averages the measurements at points 1, 2, 3, and 4. Besides, the calculated temperatures are compared with tested temperatures. Additional maximum temperature is summarized in Table IV.

The results indicate that the lowest temperature occurs at the outer surface of the core, while the maximum temperature is observed at the inner middle of the core. Similarly, the insulation's middle region exhibits significantly higher temperatures compared to the insulation end. There is convective heat transfer at the surfaces of the end insulation and the core, while the heat transfer among the winding, insulation, and core primarily occurs through thermal conduction. In the core-winding middle region, heat losses are concentrated, and heat dissipation is inefficient, leading to elevated temperatures compared to other regions. Hence, the middle region of the core and the insulation has the high temperature due to the different heat exchange mechanisms and heat source distributions. Consequently, this region is subject to a large thermal load. Furthermore, the experimental data presented in Fig. 13 (c) and (d) corroborate the calculated temperature distributions for both the core and insulation.

The influence of RISC factors on losses increases parallels the impact of temperature. As the degree of RISC increases, a corresponding rise in temperature is observed. The RISC position farther from the rotor's large teeth or a reduction in contact resistance exhibits similar trends. Consequently, the thermal load on the insulation increases. It is necessary to pay attention to the thermal aging of the insulation under the action of thermal load. Specially, compared with normal case, the insulation temperature under the RISC case with R_f 1Ω rises by 1.95°C (as per FEA) and by 3.05°C (as per experimental results). Conversely, a reduction in output leads to decreased insulation the thermal load in both FEA and experimental results, due to a significant reduction in the copper loss. Further, to validate the experimental results, the generator temperature is recorded using infrared temperature measurement equipment, as shown in Appendix. The recorded infrared temperature aligns closely with the thermocouple measurements.

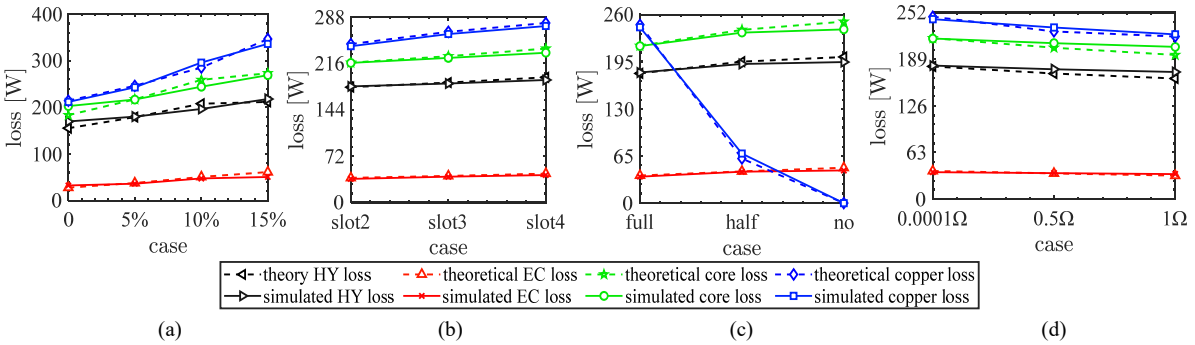

Fig. 11 Loss results by theory and FEA under different RISC cases: (a) core loss, (b) hysteresis loss, (c) eddy current loss, (d) copper loss.

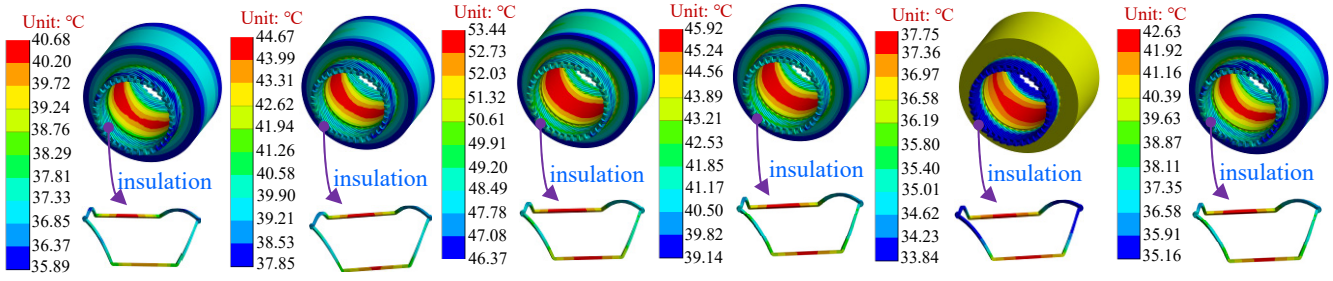

Fig. 12 Insulation temperature distribution by FEA under varied RISC cases: (a) normal (b) RISC 5% (c) RISC 15% (d) slot 3 (e) no load (f) 1 Ω

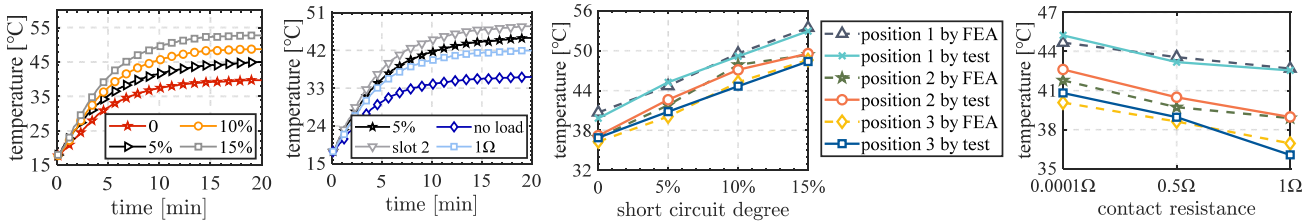

Fig. 13 Tested temperature by thermal couples: (a) insulation at P10 under different n_m, (b) insulation at P10 under other RISC cases, (c) average temperature comparison with different n_m, (d) average temperature comparison with different R_f

TABLE IV
Highest Temperature of Stator Core-Winding System under Different RISC Cases (°C)

Case	0	5%	10%	15%	Slot2	Slot3	Slot4	Full	Half	No	0.0001Ω	0.5Ω	1Ω
FEA calculation	40.68	44.67	49.59	53.44	44.67	45.92	46.84	44.67	41.26	37.75	44.67	43.56	42.63
Experiment	39.51	45.23	49.15	52.93	45.23	46.54	47.93	45.23	39.68	36.59	45.23	43.17	42.56
Error	1.17	0.56	0.44	0.51	0.56	0.62	1.09	0.56	1.58	1.16	0.56	0.39	0.07

D. Mechanical load results

Fig. 14 illustrates the EF in the winding, calculated by FEA. The winding and the insulation are closely fitted, allowing the EF to be treated as a mechanical load on the insulation. The EF harmonics are limited to DC and even harmonics under the normal case. The onset of a RISC introduces new odd harmonics in the EF. Fig. 14(a)-(d) provide compelling evidence that increasing short circuit degrees and reducing contact resistance significantly enhance the EF amplitude. Consequently, the amplitudes of the DC component, as well as 1st, 2nd, 3rd, and 4th harmonics, are all amplified. Similarly, the greater the angle of the RISC position, the greater the EF. Additionally, lower outputs correspond to diminished insulation mechanical load since the EF is closely related to phase current. The FEA results are consistent with the theoretical analysis.

Furthermore, the winding vibration, characterized by the acceleration, is measured to validate the aforementioned EF analysis. Based on the dynamical theory of mechanical system (seeing (14)), the frequency components of the vibration and the insulation load are identical. Meanwhile, the amplitude changes corresponding to each characteristic frequency can effectively and correctly reflect the variation in the mechanical load. Due to space constraints, only winding vibration results obtained by the FEA calculation and the experiment under partial RISC cases are presented in Fig. 15. Detailed harmonic amplitudes of the vibration are listed in Table V, and the time - frequency results under other RISC cases are provided in Appendix.

Ideally, only even harmonics (100Hz and 200Hz) should be present in the mechanical vibration spectrum under normal case, as shown by the FEA results (see Fig. 15(a) and (e)). However, actual measurement results (see Fig. 15(c) and (g)) show the presence of odd harmonics (50Hz and 150Hz), which arise from the operational frequency and its multiples during generator operation. When the RISC takes place, new odd harmonics appear in the spectrum by the FEA, as shown in Fig. 15(f). The amplitude of the insulation vibration intensifies due to the enhanced EF. Comparing the FEA data with the tested results, the latter is disturbed by other harmonics generated by other components, while the amplitude change trends are similar, confirming the validity of the simulation calculation. Moreover, the harmonic components and the amplitude variations of the mechanical vibration also confirm the correctness and validity of the theoretical analysis of the mechanical load on the insulation.

Moreover, analysis of the spectrum in Fig. 15 and the harmonic amplitudes in Table V indicates that increased short circuit degrees and reduced contact resistance can enhance winding vibration and its harmonic amplitude. This indicates that the mechanical load on the insulation increases based on the dynamic theory of mechanical system. Similarly, increasing the output or extending the distance of the short circuit position from the rotor's big teeth can enhance winding vibration under RISC cases.

To facilitate clearer comparisons among the proposed theorical model, FEA calculations, and experiment, the 1st and 2nd harmonic amplitudes of both the EF and the insulation vibration in varied RISC degrees and contact resistance cases are shown in Fig. 16(a)-(d). The blue curves represent the EF trend, corresponding to the left y-axis, while the red curve shows the vibration change, corresponding to the right y-axis. The graphical representations indicate that the EF and the insulation vibration exhibit similar trends across all cases. Additionally, in order to verify the accuracy of the theoretical model, only the errors between the theoretical and FEA EF results are calculated as experimentally measuring the EF is challenging. Meanwhile, the error calculation is based on the FEA value, and can be obtained by (16). The errors under all RISC cases are illustrated in Fig. 16(e) - (h). Specially, the calculated error under the no output case is 100% in Fig. 16 (g) based on (16) since the theoretical value of the EF is exactly zero. Overall, except for no output case, the errors under other RISC cases generally remain below 10%, indicating a high degree of

evaluation accuracy for the proposed theorical model. Furthermore, the experimental results depicted in Fig. 16(a) - (d) indirectly validate the correctness of the proposed model against FEA results. Theoretical model errors primarily stem from simplifications, such as neglecting leakage fields and slot effects, while inaccuracies in the FEA arise from mesh division and material parameter discrepancies.

$$E_{er} = \left| \frac{A_t - A_s}{A_s} \right| * 100\% \tag{16}$$

where E_{er} denotes the harmonic amplitude error, A_t and A_s are the theorical value and the simulation value of the harmonic amplitude, respectively.

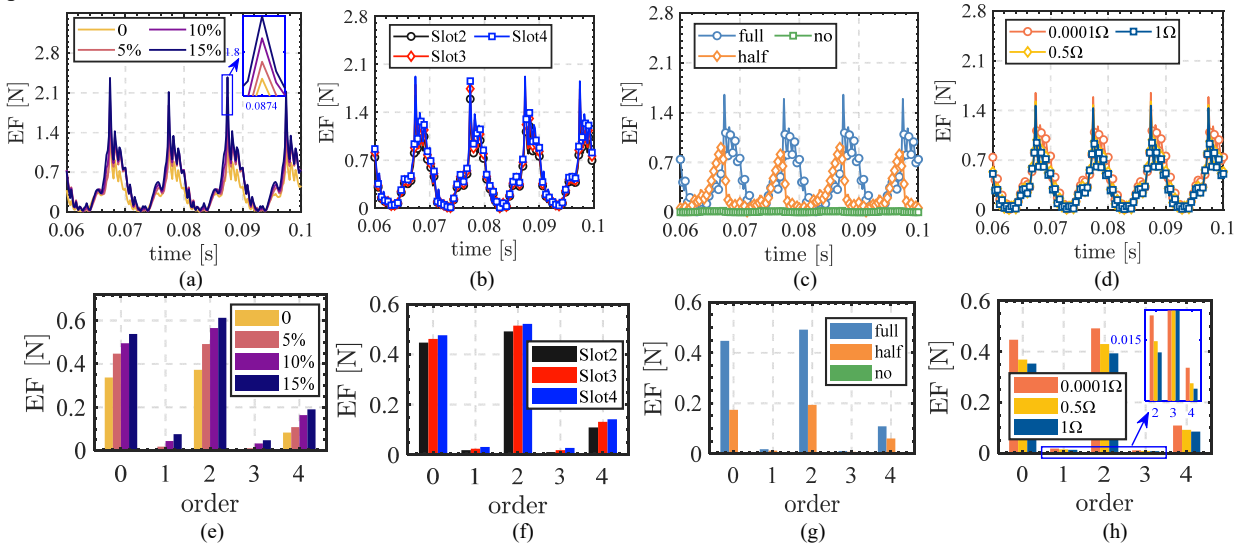

Fig. 14 EF by FEA: (a) to (d) curves and (e) to (h) spectrum under varied short circuit degrees, varied positions, varied contact resistance, varied loads

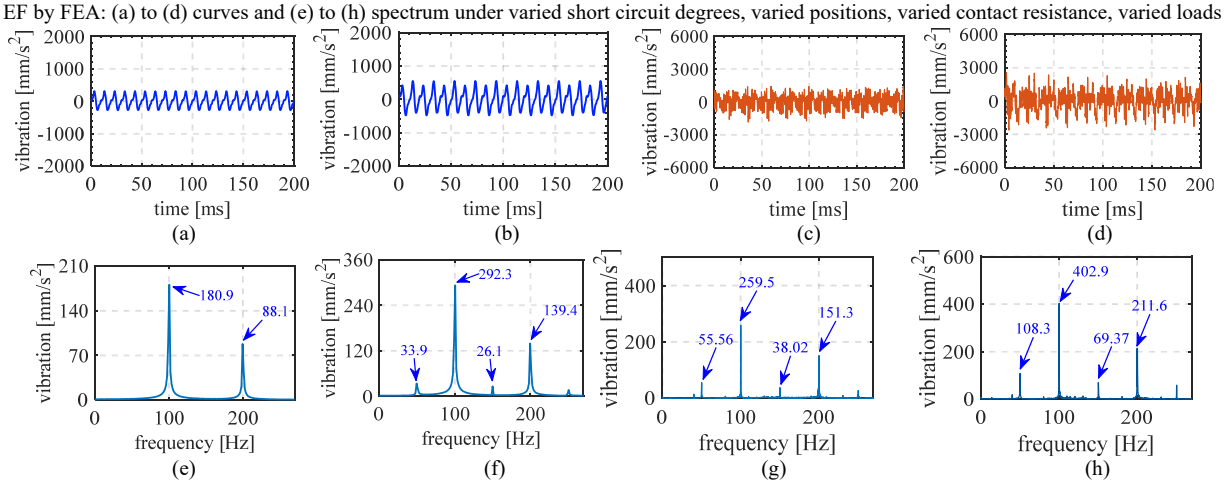

Fig. 15 Winding vibration results: (a) to (b) time curves by FEA under normal and RISC5% case, (c) to (d) time curves by experiment under normal and RISC5% case, (e) to (f) spectrum by FEA under normal and RISC5% case, (g) to (h) spectrum by experiment under normal and RISC5% case, respectively

TABLE V

Tested Vibration Harmonic Amplitudes under Different RISC Cases (mm/s²)

Case	0	5%	10%	15%	Slot2	Slot3	Slot4	Full	Half	No	0.0001Ω	0.5Ω	1Ω
1st	55.56	108.3	216	343.8	108.3	160.8	189.3	108.3	81.69	52.74	108.3	92.36	85.61
2nd	259.5	402	661.6	975.5	402	536.7	614.4	402	283.7	68.34	402	371.9	346.4
3rd	38.02	69.37	143.1	234.4	69.37	94.54	125.7	69.37	41.23	32.01	69.37	57.62	46.36
4th	151.3	211.6	363.4	451.4	211.6	273.5	332.2	211.6	84.39	63.94	211.6	189.3	163.3

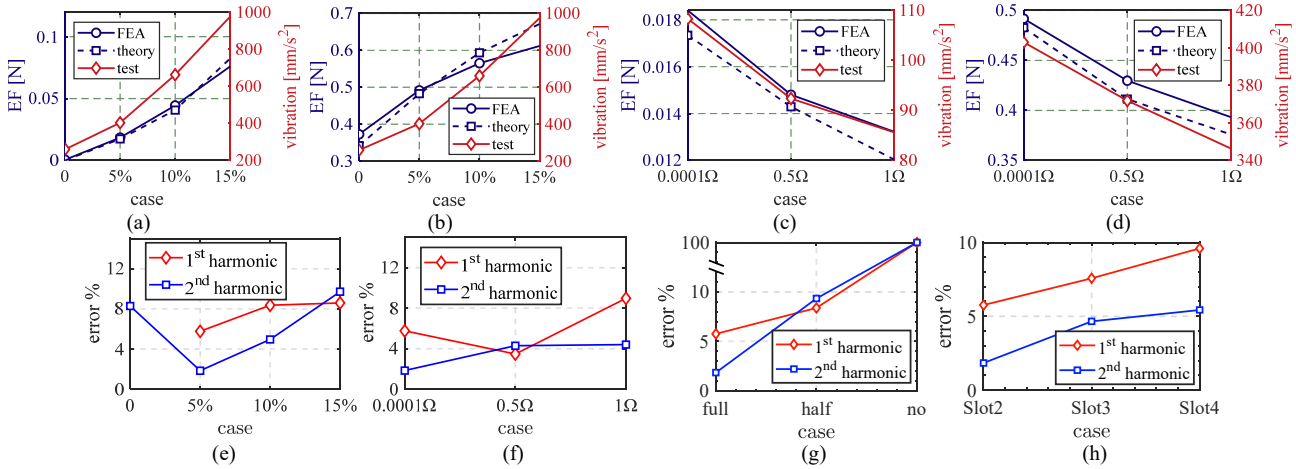

Fig. 16 EF and winding vibration comparison: (a) 1st and (b) 2nd harmonic amplitude with different short circuit degrees, (c) 1st and (d) 2nd harmonic amplitude with varied contact resistances, (e) to (h) EF results error under different RISC degrees, contact resistances, outputs and positions, respectively

E. Insulation structural responses based on thermal, mechanical and coupling loads

Fig. 17 presents the mechanical, thermal, and coupling structural responses of the insulation under the RISC 5% case. Due to space limitations, additional responses amplitudes under various RISC cases are provided in Table VI. The results of the insulation structural responses under some cases are presented in Appendix. Furthermore, to elucidate detrimental impact of different stress types on insulation, stress variation over time is illustrated in Fig. 18.

Based on the distribution and the maximum amplitude variations of structural responses, the maximum deformation occurs at the insulation nose end in most RISC cases, whereas, under no-output cases, the maximum deformation is observed at the junction of the straight segment and the involute. This behavior can be attributed to the insulation end being a cantilever beam structure, which experiences dislocation displacement at the furthest nose end. In contrast, under no-output cases, the thermal load on the winding primarily originates from the stator core. Thus, at the junction of the insulation, stator core, and air-i.e., the connection point-there is the largest temperature differential, resulting in the greatest thermal deformation. Additionally, the maximum insulation stress is located at the junction due to alterations in the insulation structure. Consequently, the nose end and the junction of the insulation, under the influence of mechanical and thermal loads, are important areas warranting special attention.

Moreover, when the RISC occurs, three stresses values increase compared to the normal case considering the full output. Meanwhile, the results show that the occurrence of RISC amplifies the load on the insulation based on (15). Under the RISC cases, the mechanical, thermal, and coupling responses increase with heightened short circuit degrees, increased distance of the short circuit from the rotor's big teeth, increased output, and reduced contact resistance. Therefore, it is essential to detect short circuit faults timely to prevent the additional load on the stator winding insulation, which could result in the possible shortening of the insulation service life.

Besides, it is imperative to note that the amplitude of the thermal response significantly exceeds that of the mechanical response, yet remains smaller under single actions compared to coupling action. However, this does not imply that the thermal load on the insulation is more harmful than the mechanical load. The mechanical stress experienced by the insulation is dynamic and high-frequency, while the thermal stress is static and stabilizing once the insulation temperature stabilizes, as shown in Fig. 18(a) and (b). This also shows from the side that the mechanical load is dynamic, while the thermal load is constant, which accords with the above analysis results. Consequently, despite the smaller amplitude of mechanical stress, it can still inflict considerably negative impact on the insulation. The stress experienced under coupling action combines the characteristics of both individual stress types. Therefore, analyzing only a single load action is neither comprehensive nor adequate for investigating the structural responses characteristics of the insulation. Consequently, improving insulation performance should focus not only on enhancing thermal load-bearing capacity of insulation materials at important locations but also on increasing fatigue strength of the insulation.

The analysis indicates significant deformation and stress concentration at specific positions, which are particularly pronounced at the nose end and the junction. Fig. 19 depicts insulation damage observed under field scenes following prolonged operation. Generally, the insulation damage locations correlate with maximum structural response position. Thus, directing attention to these important areas is essential.

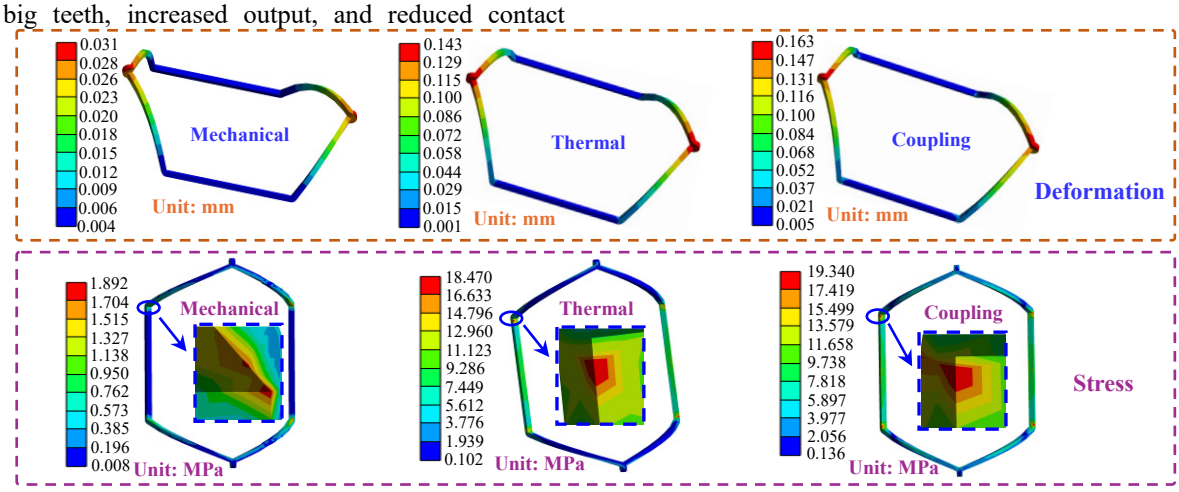

Fig. 17 Insulation structural responses under RISC 5% case

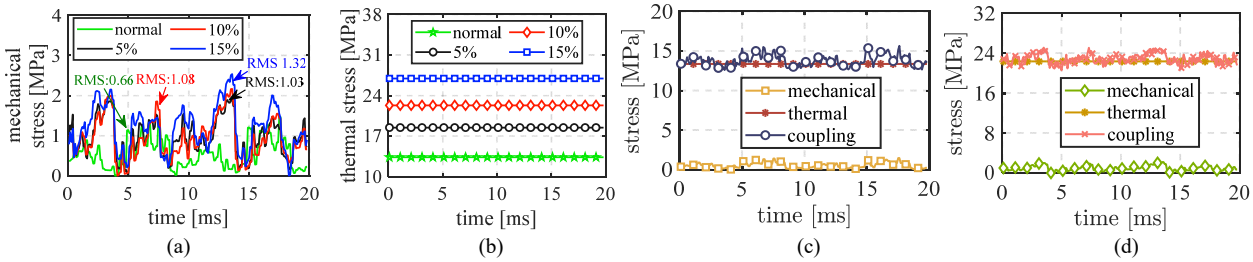

Fig. 18 Insulation stress curves: (a) mechanical stress, (b) thermal stress, (c) three stresses under normal, (d) three stresses under RISC 5%

TABLE VI
Insulation Structural Response Amplitudes under Different RISC Cases

Case		0	5%	10%	15%	Slot2	Slot3	Slot4	Full	Half	No	0.0001Ω	0.5Ω	1Ω
Deformation (mm)	Thermal	0.098	0.143	0.189	0.204	0.143	0.161	0.172	0.143	0.103	0.058	0.143	0.131	0.119
	Mechanical	0.021	0.031	0.039	0.048	0.031	0.035	0.037	0.031	0.014	$6*10^{-5}$	0.031	0.028	0.025
	Coupling	0.121	0.163	0.191	0.223	0.163	0.179	0.196	0.163	0.109	0.061	0.163	0.15	0.138
Stress (MPa)	Thermal	13.36	18.47	22.31	26.95	18.47	19.38	21.17	18.47	14.95	9.342	18.47	16.86	15.03
	Mechanical	1.467	1.892	2.164	2.537	1.892	1.991	2.068	1.892	7.627	$4*10^{-5}$	1.892	1.703	1.594
	Coupling	14.91	19.34	23.85	28.73	19.34	21.66	23.08	19.34	15.28	9.361	19.34	18.31	16.52

Fig. 19 Pictures of nose and joint damage

IV. Conclusion

This paper investigates the thermal and mechanical load characteristics of winding insulation under RISC cases, along with the structural responses of insulation under single and coupled loads. The deformation and stress distributions of the insulation under double loads are delineated, and the increasing effect of the RISC on insulation structural responses is examined. The principal conclusions of this work are as follows.

1) The thermal load on winding insulation is greatest in the straight section and least at the end. The occurrence of the RISC increases the thermal load on the insulation, with the thermal response predominantly in a steady state.

2) The mechanical load borne by insulation is dynamic, primarily exhibiting the 2nd and 4th harmonics, while the 1st and 3rd harmonics occur in the presence of the RISC.

3) The insulation loads under RISC cases are influenced by four factors. RISC degree intensification, an increase in the distance of the RISC position from the rotor big teeth, reduced contact resistance, and increased output, all of which contribute to elevate the mechanical and thermal loads on the insulation.

4) Important points, which exhibit maximum structural responses of the insulation, are identified, particularly at the nose end and the junction between the straight segment and the involute section. Applying a high-temperature and fatigue-resistant coating to these points or adding a sheath capable of withstanding significant loads could extend the likelihood of insulation service life.

In conclusion, this paper provides comprehensive investigation into the mechanical and thermal loads experienced by winding insulation, offering the reference and basis for insulation load evaluation of electric machines in real scenarios. The findings have significant potential as a foundation for addressing related insulation load issues in other similar electrical machines. Concurrently, this study is helpful in formulating effective and straightforward strategies to enhance the insulation reliability and extend its service life.

V. Appendix

Temperature distribution of the synchronous generator by infrared sensor is shown in Fig. 20 under varied RISC fault.

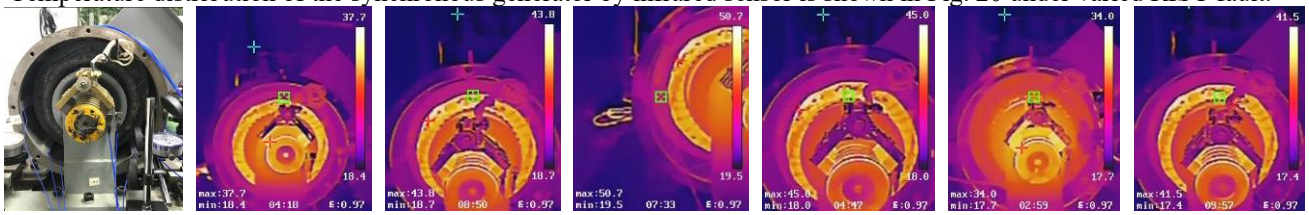

Fig. 20 Temperature distribution by infrared sensor under varied RISC fault: (a) reference contour (b) normal (c) 5% (d) 15% (e) slot 3 (f) no output (g) 1 Ω

The time curves and the frequency domain spectrum of the insulation vibration, as obtained from the FEA calculations and the experiment under some RISC cases, are shown in Fig. 21 and Fig. 22, respectively. Specially, the insulation vibration predicted by the FEA under no output case is essentially zero because no EF on the insulation is present.

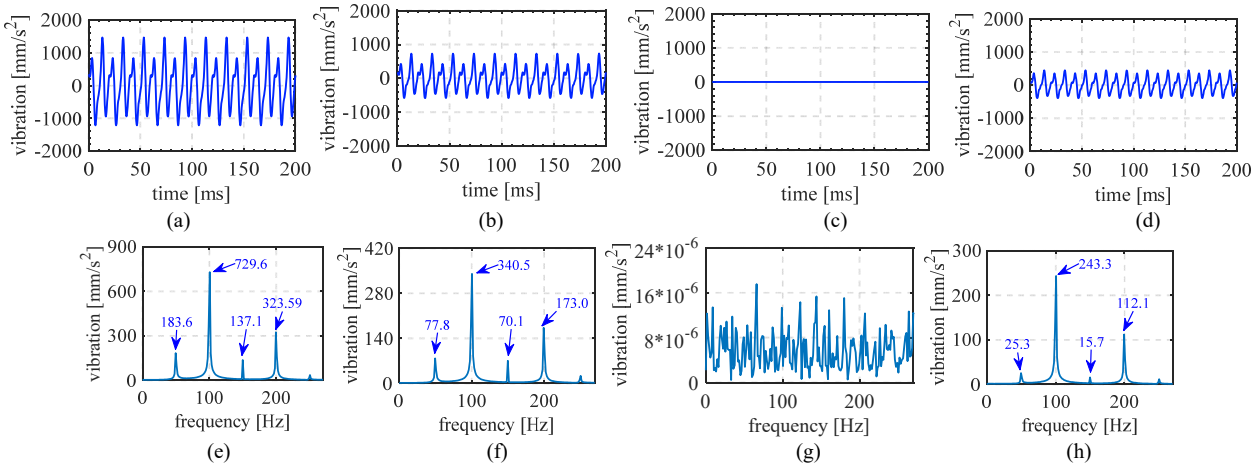

Fig. 21 Insulation vibration by FEA calculation: (a) to (d) time curves, (e) to (h) spectrum under RISC case with 15%, slot 3, no output and 1Ω, respectively

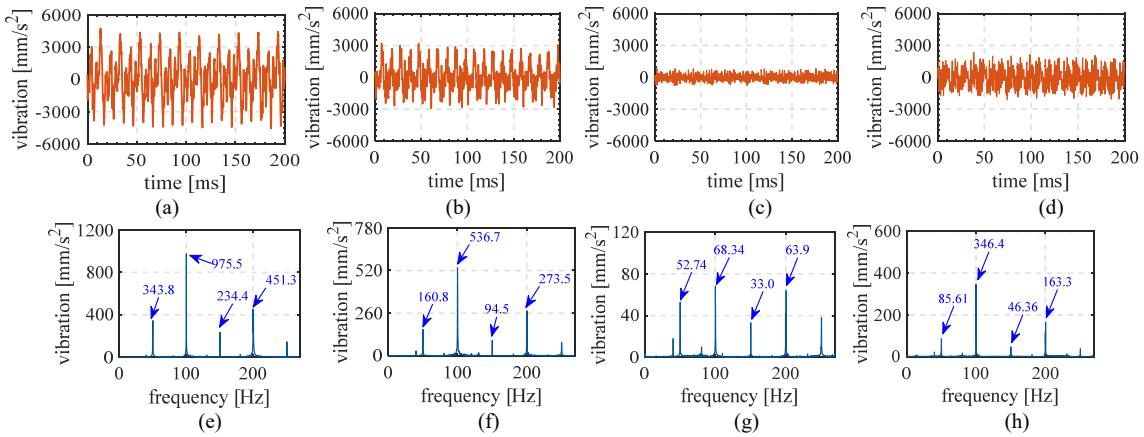

Fig. 22 Tested insulation vibration: (a) to (d) time curves, (e) to (h) spectrum under RISC case with 15%, slot 3, no output and 1 Ω, respectively

The structural responses of the insulation under the normal, the RISC 15% and the no load cases are provided in Fig. 23.

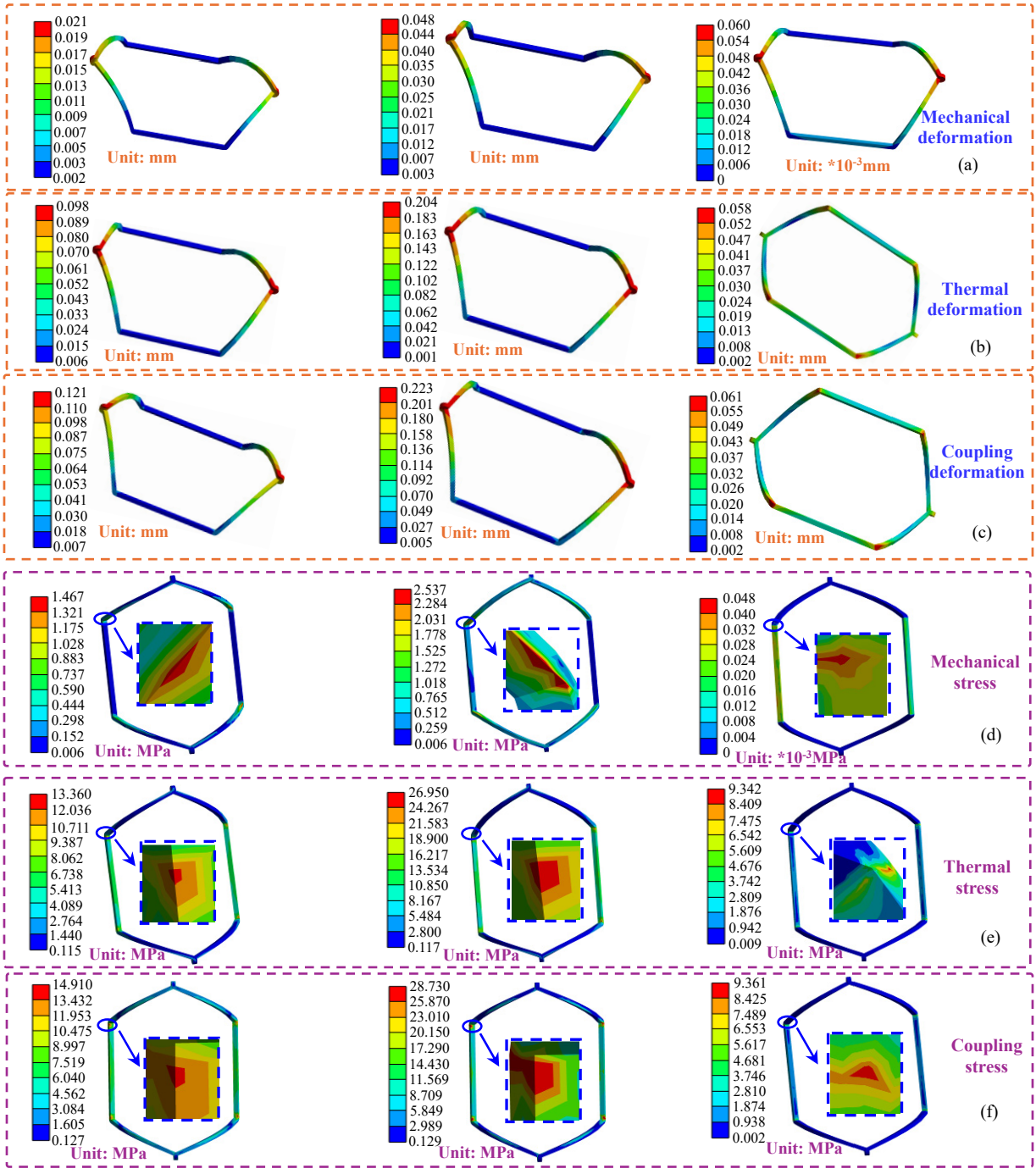

Fig. 23 Insulation responses under normal, RISC 15% and no load (left to right): (a) mechanical deformation, (b) thermal deformation, (c) coupling deformation, (d) mechanical stress, (e) thermal stress, (f) coupling stress

REFERENCES

[1] M. Valavi, K. G. Jørstad and A. Nysveen, "Electromagnetic Analysis and Electrical Signature-Based Detection of Rotor Inter-Turn Faults in Salient-Pole Synchronous Machine," in IEEE Transactions on Magnetics, vol. 54, no. 9, pp. 1-9, Sept. 2018, Art no. 8104309.

[2] H. Lee, H. Jeong, G. Koo, J. Ban and S. W. Kim, "Attention Recurrent Neural Network-Based Severity Estimation Method for Interturn Short-Circuit Fault in Permanent Magnet Synchronous Machines," in IEEE Transactions on Industrial Electronics, vol. 68, no. 4, pp. 3445-3453, April 2021.

[3] Zamudio-Ramirez, R. A. Osornio-Rios, J. A. Antonino-Daviu, et al., "Magnetic Flux Analysis for the Condition Monitoring of Electric Machines: A Review," in IEEE Transactions on Industrial Informatics, vol. 18, no. 5, pp. 2895-2908, May 2022.

[4] C. E. G. Guillén, A. M. de Porras Cosano, P. Tian, J. C. Diaz, A. Zarzo and C. A. Platero, "Synchronous Machines Field Winding Turn-to-Turn Fault Severity Estimation Through Machine Learning Regression Algorithms," in IEEE Transactions on Energy Conversion, vol. 37, no. 3, pp. 2227-2235, Sept. 2022.

[5] K. B. Jamdade and A. R. Thorat, "Novel on-line field ground-fault location method for alternators with static excitation," 2014 International Conference on Circuits, Power and Computing Technologies, Nagercoil, India, 2014, pp. 1065-1069.

[6] H. Ehya, T. N. Skreien and A. Nysveen, "Intelligent Data-Driven Diagnosis of Incipient Interturn Short Circuit Fault in Field Winding of Salient Pole Synchronous Generators," in IEEE Transactions on Industrial Informatics, vol. 18, no. 5, pp. 3286-3294, May 2022.

[7] B. Aubert, J. Régnier, S. Caux and D. Alejo, "Kalman-Filter-Based Indicator for Online Interturn Short Circuits Detection in Permanent-Magnet Synchronous Generators," in IEEE Transactions on Industrial Electronics, vol. 62, no. 3, pp. 1921-1930, March 2015.

[8] L. Hao, Y. Sun, A. Qiu and X. Wang, "Steady-State Calculation and Online Monitoring of Interturn Short Circuit of Field Windings in Synchronous Machines," in IEEE Transactions on Energy Conversion, vol. 27, no. 1, pp. 128-138, March 2012.

[9] H. Ehya and A. Nysveen, "Pattern Recognition of Interturn Short Circuit Fault in a Synchronous Generator Using Magnetic Flux," in IEEE Transactions on Industry Applications, vol. 57, no. 4, pp. 3573-3581, July-Aug. 2021.

[10] M. Cuevas, R. Romary, J. -P. Lecointe and T. Jacq, "Non-Invasive Detection of Rotor Short-Circuit Fault in Synchronous Machines by Analysis of Stray Magnetic Field and Frame Vibrations," in IEEE Transactions on Magnetics, vol. 52, no. 7, pp. 1-4.

[11] S. Toma, L. Capocchi and G. -A. Capolino, "Wound-Rotor Induction Generator Inter-Turn Short-Circuits Diagnosis Using a New Digital Neural Network," in IEEE Transactions on Industrial Electronics, vol. 60, no. 9, pp. 4043-4052, Sept. 2013.

[12] S. Zhao et al., "Detection of Interturn Short-Circuit Faults in DFIGs Based on External Leakage Flux Sensing and the VMD-RCMDE Analytical Method," in IEEE Transactions on Instrumentation and Measurement, vol. 71, pp. 1-12, 2022, Art no. 3516312.

[13] G. Lian, H. Li, B. Chen, F. Ban and J. Zhang, "Characteristic Analysis and Temperature Rise Calculation of PMSM Under Different Power Supply Modes," in IEEE Transactions on Applied Superconductivity, vol. 29, no. 2, pp. 1-5, March 2019.

[14] Y. -L. He et al., "Impact of Static Air-Gap Eccentricity on Thermal Responses of Stator Winding Insulation in Synchronous Generators," in IEEE Transactions on Industrial Electronics, vol. 69, no. 12, pp. 13544-13554, Dec. 2022.

[15] J. Wang, M. Cheng, W. Qin and Q. Liu, "Fast Calculation Method of Bi-Direction Coupling Between Electromagnetic-Thermal Field for FSPM Motor," in IEEE Transactions on Magnetics, vol. 59, no. 12, pp. 1-9, Dec. 2023, Art no. 8205909.

[16] S. Jia, R. Qu, J. Li, X. Fan and M. Zhang, "Study of Direct-Drive Permanent-Magnet Synchronous Generators with Solid Rotor Back Iron and Different Windings," in IEEE Transactions on Industry Applications, vol. 52, no. 2, pp. 1369-1379, March-April 2016.

[17] R. Wrobel, A. Mlot and P. H. Mellor, "Contribution of End-Winding Proximity Losses to Temperature Variation in Electromagnetic Devices," in IEEE Transactions on Industrial Electronics, vol. 59, no. 2, pp. 848-857, Feb. 2012.

[18] G. Berardi and N. Bianchi, "High-Speed PM Generators for Organic Rankine Cycle Systems: Reduction of Eddy Current Rotor Losses," in IEEE Transactions on Industry Applications, vol. 55, no. 6, pp. 5800-5808, Nov.-Dec. 2019.

[19] W. Li, H. Qiu, X. Zhang, J. Cao and R. Yi, "Analyses on Electromagnetic and Temperature Fields of Superhigh-Speed Permanent-Magnet Generator With Different Sleeve Materials," in IEEE Transactions on Industrial Electronics, vol. 61, no. 6, pp. 3056-3063, June 2014.

[20] L. Weili, H. Jichao, Z. Xingfu and L. Yong, "Calculation of Ventilation Cooling, Three-Dimensional Electromagnetic Fields, and Temperature Fields of the End Region in a Large Water–Hydrogen–Hydrogen-Cooled Turbogenerator," in IEEE Transactions on Industrial Electronics, vol. 60, no. 8, pp. 3007-3015, Aug. 2013.

[21] W. Su, D. Wang, Y. Guo and Z. Su, "The DMCM-Based Analytical Calculation of Radial Vibration Force in a Nonsalient Pole Synchronous Generator in No-Load Conditions," in IEEE Transactions on Industrial Electronics, vol. 66, no. 7, pp. 5364-5373, July 2019.

[22] Wen Zhang, Yu-Ling He, Ming-Xing Xu, et al., "A comprehensive study on stator vibrations in synchronous generators considering both single and combined SAGE cases," in International Journal of Electrical Power & Energy Systems, Vol. 143, 2022, 108490.

[23] Z. Song, C. Liu, H. Zhao and R. Huang, "Nonlinear Force and Vibration Analysis of an Interior Permanent Magnet Synchronous Generator with Eccentricity Detection," in IEEE/ASME Transactions on Mechatronics, vol. 27, no. 5, pp. 2545-2555, Oct. 2022.

[24] Y. -L. He et al., "Comprehensive Analysis on Rotor Vibration Characteristics Based on a Novel Dynamic Stator Interturn Short Circuit Model of Synchronous Generator," in IEEE Transactions on Energy Conversion, vol. 39, no. 3, pp. 1658-1672, Sept. 2024.

[25] Y. -L. He et al., "Impact of Stator Interturn Short Circuit Position on End Winding Vibration in Synchronous Generators," in IEEE Transactions on Energy Conversion, vol. 36, no. 2, pp. 713-724.

[26] Wan Shuting, Li Yonggang, Li Heming and Tang Guiji. "The new diagnosis method of rotor winding inter-turn short circuit fault and imbalance fault based on stator and rotor vibration characteristics". in 2005 International Conference on Electrical Machines and Systems 2005. pp. 2207-2210.

[27] Y. Zhou and G. Yang. "Transient response analysis of short-circuit electromagnetic force on the rotor teeth of a high-speed generator". in: 2021 IEEE 4th International Electrical and Energy Conference (CIEEC) 2021. pp. 1-6.

[28] Y. -L. He et al., "A Novel Universal Model Considering SAGE for MFD-Based Faulty Property Analysis Under RISC in Synchronous Generators," in IEEE Transactions on Industrial Electronics, vol. 69, no. 7, pp. 7415-7427, July 2022.

[29] Y. -L. He et al., "Effect of RISC Positions on End Winding Vibrations in Synchronous Generators," 2022 International Conference on Sensing, Measurement & Data Analytics in the era of Artificial Intelligence, Harbin, China, 2022, pp. 1-6.

[30] H. C. Dirani, A. Merkhouf, B. Kedjar. A. -M. Giroux and K. Al-Haddad, "Rotor interturn short circuit impact on large hydrogenerator magnetic quantities". IEEE Transactions on Industry Applications ,2018: 54(4): 3702-3711.

[31] L. Zhang and Y. Liang, "Circuit Network Method of Short Circuit Fault Between Transposed Strands for Large Turbo-Generators," in IEEE Transactions on Energy Conversion, vol. 38, no. 4, pp. 2762-2771, Dec. 2023, doi: 10.1109/TEC.2023.3287407.

[32] Y. Wu, X. Fan, L. Xu, P. Qi and W. Lu, "Detection of Field Coil Short-Circuit Fault in Synchronous Generators Based on Magnetic Bypass Shunt Effect," in IEEE Transactions on Industrial Electronics, vol. 71, no. 9, pp. 11498-11507, Sept. 2024.

[33] WU Yu-cai, Li Hong-shuo, WANG Ze-lin, et al., "Hazard assessment of short circuit fault in excitation winding of turbogenerators under extremely unfavorable condition," in Electric Machines and Control, vol. 25, no. 10, pp. 9-20, Dec. 2021, doi: 10.15938/j.emc.2021.10.002.

[34] Y. Tai, and Z. Liu, “Analysis on Three-dimensional Transient Temperature Field of induction Motor,” in Proceedings of the CSEE, vol. 30, no. 30, pp. 114-120, 2010. Doi: 10.13334/j.0258-8013.

[35] LIN Juguan, LAI Jianbi, LU Ling, "Thermal-structural coupled analysis of the rotor of vehicle permanent magnet synchronous motor," in Journal of Hefei University of Technology, vol. 42, no. 7, pp. 172-177, 2019.